www.sciencemag.org/content/353/6299/594/suppl/DC1

Supplementary Materials for

The inhibition mechanism of human 20*S* proteasomes enables next-generation inhibitor design

Jil Schrader, Fabian Henneberg, Ricardo A. Mata, Kai Tittmann, Thomas R. Schneider, Holger Stark, Gleb Bourenkov,* Ashwin Chari*

*Corresponding author. Email: ashwin.chari@mpibpc.mpg.de (A.C.); gleb@embl-hamburg.de (G.B.)

Published 5 August 2016, *Science* **353**, 594 (2016)
DOI: 10.1126/science.aaf8993

This PDF file includes:

Other Supplementary Material for this manuscript includes the following:
(available at www.sciencemag.org/cgi/content/full/353/6299/594/DC1)

Materials and Methods

Materials

Standard chemicals were obtained from Sigma Aldrich (Taufkirchen, Germany). The proteasome inhibitors Oprozomib, Epoxomicin and Dihydroeponemycin were purchased from ApexBio (Houston, USA), MLN9708 and Bortezomib were obtained from Selleck Chemicals (Munich, Germany) and Z-LLY-Ketoaldehyde from Bachem (Bubendorf, Switzerland), and were resuspended in DMSO at 100 mM concentration. Detergents were obtained from Anatrace (Maumee, USA), crystallization plates from Hampton Research (Aliso Viejo, USA), Litholoops from Molecular Dimensions (Suffolk, UK) and Jena Bioscience (Jena, Germany).

Methods

Purification of human 20S proteasomes

S30 HeLa cytoplasmic extract was prepared by hypotonic lysis according to Dignam et al. (*20*), with some minor modifications: after hypotonic lysis and centrifugation to collect nuclei, the supernatant (the crude cytoplasmic extract) was centrifuged at 30´000 x g for 30 minutes at 4°C and flash frozen in 40 ml aliquots in liquid nitrogen and stored at -80 °C until further use. The S30 HeLa cytoplasmic extract was thawed in a water bath at 37 °C, supplemented with purification buffer to 1x concentration from a 10x stock, followed by the addition of sucrose powder to 20 % (w/v), Octyl Glucose Neopentyl Glycol (OGNG; from a 10 % (w/v) stock solution in water) to 0.1 % (w/v), Iodacetamide to 10 mM, *N*-Ethylmaleimide to 10 mM and Benzamidine Chloride to 10 mM. The extract was incubated at room temperature on a magnetic stirrer for 30 minutes, followed

by incubation at 30 °C with shaking at 140 rpm for 1 hour. The treated extract was centrifuged at 100´000 x g for 2 hours at 4°C. After centrifugation, the supernatant was filtered through 3 layers each of cheese cloth and miracloth to obtain a S100 HeLa cytoplasmic extract.

The clarified extract is subjected to differential precipitation with PolyEthyleneGlycol400 (PEG; number signifies the mean molecular weight of the PEG polymer). PEG400 is added to a concentration of 20 % (v/v) to the S100 HeLa cytoplasmic extract under stirring at 4 °C and incubated for 20 minutes. Precipitated proteins are removed by centrifugation at 30,000 x g for 30 minutes at 4 °C. The supernatant is then precipitated by raising the concentration of PEG400 to 30 % (v/v) as described above. The precipitate of this step, which contains human 20S proteasomes, is recovered by centrifugation at 30,000 x g for 30 minutes at 4 °C and resuspended in purification buffer containing 2 % (w/v) sucrose, 10 mM DTT and 0.01 % (w/v) Lauryl Maltose Neopentyl Glycol (LMNG) in an orbital shaker at 18 °C. The resuspended material is loaded on 10-30 % (w/v) sucrose gradients in purification buffer containing 5 mM DTT, which are centrifuged at 270,000 x g for 16 h at 4 °C. Gradients were harvested in 400 µl fractions with Äkta Prime™ (GE Healthcare, Munich, Germany). SDS-PAGE was utilized to identify fractions containing 20S proteasomes. Selected fractions were pooled and precipitated by the addition of 40 % (v/v) PEG400. After centrifugation (30,000 xg, 20 minutes), the supernatant was removed and the precipitate was resuspended in purification buffer containing 5 % (w/v) sucrose, 10 mM DTT and 0.01 % (w/v) LMNG. The resuspended material is loaded on linear 10-40 % (w/v) sucrose gradients in purification buffer containing 5 mM DTT, which are centrifuged at

284,000 x g for 20 h at 4 °C. Fractions containing 20S proteasomes are yet again identified by SDS-PAGE, precipitated and concentrated by the addition of 40 % PEG400 and resuspended in purification buffer containing 5 % (w/v) sucrose, 5 mM DTT and 0.01 % LMNG, yielding the final purified protein preparation at 13 mg/ml. Protein concentrations were determined by the Bradford assay (BioRad, Munich, Germany) using BSA as a standard. This procedure reproducibly yields 20 mg purified human 20S proteasomes, starting from 300 ml S100 HeLa cytoplasmic extract at a concentration of 10 mg/ml. The entire purification procedure is concluded within 48 hours yielding crystallization grade protein.

Crystallization of human 20S proteasomes

Human 20S proteasomes are crystallized at a protein concentration of 7.5 mg/ml by mixing 0.5 µl protein + 0.5 µl Crystallization buffer in Chryschem sitting drop vapor diffusion plates (Hampton Research, Aliso Viejo, USA) over a 500 µl reservoir of Crystallization buffer. Under these conditions, human 20S proteasomes purified by the procedure described herein crystallize in space group $P2_12_12_1$ with unit cell constants a= 114Å, b= 202Å, c= 302Å, α= β= γ= 90°. The purification procedure described above is therefore suitable to typically perform in excess of 5,000 crystallization setups. Additional advantages of the presently identified crystallization conditions include that each crystallization setup typically yields 10- 15 crystals, which are 150x 150 x 200 μm^3 in size. Crystal growth to full size of the crystals is achieved within 20 hours of incubation (see Figure1). Hence, ~50,000 crystals can be generated within 72 hours of extract preparation that all typically diffract to resolutions below 2.2 Å.

Crystal stabilization and dehydration

Human 20S proteasome crystals obtained by the procedures described above need to be stabilized and dehydrated in a controlled manner to reproducibly diffract to resolutions below 2.2 Å. We have spent considerable effort to establish reproducible procedures to achieve this. Three steps are involved: 1) Crystallization trays containing human 20S crystals initially grown at 18 °C, are placed into Styrofoam boxes and transferred to 4 °C. The trays are typically incubated for 8 hours. 2) The crystals are stabilized and dehydrated at 4 °C. Initially, seals are removed and 1 µl of reservoir solution is added. Then 2 µl of the crystal stabilization buffer is added to the crystallization drop. At the same time the reservoir solution is exchanged to crystal dehydration buffer. The drops are then re-sealed and allowed to equilibrate against the new reservoir solution by vapor diffusion in excess of 8 hours at 4 °C. 3) Proteasome inhibitors are soaked into the crystals by the addition of 4 µl of Crystal dehydration buffer to the drops, which additionally contains 5 mM of the proteasome inhibitor of choice (final concentration: 2.5 mM). The drops are then resealed and allowed to equilibrate in excess of 12 hours. The entire crystal stabilization, dehydration and ligand soaking procedures are therefore concluded within 30 hours.

Diffraction data collection

At this stage human 20S proteasome crystals are ready for harvest and data collection. To achieve this, crystals are harvested in Litholoops (Molecular dimensions, Suffolk, UK or Jena Bioscience, Jena, Germany) mounted on magnetic pins and vitrified

by either plunge-cooling in liquid nitrogen or direct transfer to a nitrogen gas stream at 100 K. Data collection occurs under cryogenic conditions at 100 K. Initial data collections of human 20S proteasome crystals were performed at beamline ID23-1, ESRF, Grenoble, France. All high-resolution diffraction datasets reported in this manuscript were collected on EMBL beamline P14 at the PETRA III storage ring (DESY, Hamburg, Germany) using a MD3 vertical-spindle diffractometer (EMBL and Arinax, Moirans, France) and a PILATUS2 6MF detector (Dectris, Baden, Switzerland). The X-ray beam as produced by the undulator was defined by a white-beam compound refractive lense transfocator positioned 20.6 m upstream of the sample position, imaging the X-ray source at 3 to 4 m downstream of the sample, and by slits 0.3 m upstream of the sample. Under these conditions, a smooth, "top-hat" beam profile with a total photon flux of up to 2x 10^{13} ph/ sec was created. Using different slit settings, beam sizes between 150 - 200 μm^2 in linear dimensions – matching the crystal dimensions - were created. In our hands, for the large and well-ordered three-dimensional crystals of the human 20S proteasome, this classical "bathing-the-crystal" approach provided far superior data sets in comparison to multi-positional and/or or helical data collection strategies employing standard setups with the X-ray beam focused into a 20-50 μm spot on a larger sample - for the latter cases the maximum resolution we were able to obtain was only 2.3 Å resolution.

Diffraction data were typically collected using 40 ms exposures, φ-slicing of 0.05-0.10, and a total rotation range of 180°-360° at 50 % attenuation. A full dataset is therefore collected in less than 5 minutes. In general, by following these procedures diffraction data can be collected to better than 2.2 Å resolution using crystals obtained

with the crystallization, dehydration and stabilization conditions described above. Diffraction data are rapidly scaled and integrated with the XDS program package (*21*) using standard protocols within minutes after data collection.

Structure determination

Initial phases for human 20S proteasomes were determined by molecular replacement using the murine 20S structure (PDB ID: 3UNE). The model was built and optimized by several rounds of interactive manual model building in Coot (*22*) and refinement in Refmac5 (*23*). The obtained structures display excellent stereochemistry with typical values for R_{work}= 18 % and R_{free}= 21 % (Table S2), reveal very well defined electron densities essentially over the whole 20S particle. The N-terminal residues of some α subunits are disordered in our structures (α1: 1 residue, α4: 8 residues, α5: 3 residues and α6: 5 residues). The density maps revealed several ligands, which were present in buffers used for purification and crystallization (Table S1).

The identity of many ions was validated by anomalous difference Fourier maps in native crystals. When necessary soaking experiments, where the ligands in question were exchanged for anomalous scatterers, were performed: e.g., Cl^- ions were identified by their anomalous Fourier differences at 6.5 keV and by exchange through soaking crystals with Br^- ions and measurements at the bromide K- absorption edge (13.47 keV); Mg^{2+} ions were identified by exchange through soaking crystals with Mn^{2+} ions and measurement at the manganese absorption edge (6.5 keV); K^+ ions were identified by their residual anomalous scattering at 6.5 keV, non-exchangeability with either Br^- or Mn^{2+}, and via coordination distances to neighboring groups in the crystal structure. In

addition to various ionic species, more than 3,500 localized water molecules are visible in a typical crystal structure.

For modeling the bound inhibitors, complete stereo-chemical descriptions of double- or single- covalent link attachments were created using program JLigand (*23*) and applied in real-space fitting with Coot (*22*) followed by refinement with Refmac (*24*). With the availability of this excellent model for human 20S proteasomes, now structure determination can occur within minutes by refinement of the reference model against integrated and scaled X-ray data from related crystals. Bound ligands can then be rapidly identified in difference density maps and modeled interactively in Coot (*22*).

Electronic structure calculations

Cluster calculations were carried out on selected model systems, considering the Dihydroeponemycin, Oprozomib and Z-LLY-Ketoaldehyde inhibitors. The starting structures were based on the crystallographic data. All stationary points and constrained optimizations were carried out at the B3LYP-D3(BJ)/def2-SVP level of theory (*25-28*), which include dispersion corrections as suggested by Grimme, with a Becke-Johnson type damping (*29*). The nature of the stationary points was confirmed by frequency calculations. The reaction energy profiles are provided at the level of theory used for the optimizations (B3LYP-D3/def2-SVP).

Free-energy corrections were computed from frequency analysis under the rigid-rotor harmonic approximation of the latter structures. The electronic energy was determined at the B3LYP-D3/def2-TZVP level of theory, under the COSMO continuum solvation model (*30*). Diethyl ether was employed as the solvent (ε=4.3), which is

commonly chosen to model protein-like environments (*31*). All free-energy values reported correspond to the sum of the latter electronic energies and the thermodynamic corrections computed with the smaller def2-SVP basis set. All calculations were carried out with the Orca 3.0.3 program package (*32*).

Enzyme kinetics

All kinetic measurements were performed using a FluoroMax®-4 fluorescence spectrophotometer (Horiba Scientific). Succinyl-Leucine-Leucine-Valine-Tyrosine-7-amido-4-methylcoumarin (Suc-LLVY-AMC, Bachem) was used as substrate to determine the chymotryptic-like activity of the β5 catalytic active site of the human 20S proteasome (*33*). The fluorescence emission of hydrolyzed AMC was continuously monitored at 460 nm (λ_{ex} = 380 nM). The reaction temperature was kept at 37°C for all measurements and the reaction buffer for enzymatic assays specified in Table S1 was used. Suc-LLVY-AMC and inhibitors (Oprozomib, Dihydroeponemycin, Z-LLY-Ketoaldehyde) were dissolved in DMSO and stored at -80 °C until usage. The DMSO concentration did not exceed 2% (v/v) in any measurement.

For kinetic characterization of Suc-LLVY-AMC conversion, 0.035 mg/mL (50 nM) human 20S proteasome in reaction buffer was pre-incubated for 3 minutes at 37 °C. The reaction was started by the addition of substrate and the fluorescence signal was measured continuously. For determination of the first-order rate constant of inhibition of the respective inhibitors in Figure 4E, the reaction mixture containing reaction buffer, 150 µM substrate and either Oprozomib (50 µM), Dihydroeponemycin (50 µM) or Z-LLY-Ketoaldehyde (15 µM) were pre-incubated at 37 °C for 3 minutes. The reaction was

then started by the addition of human 20S proteasome to a final concentration 50 nM. The fluorescence signal was measured continuously.

Data were analyzed and fitted with OriginPro 9.1 (OriginLab) and KaleidaGraph 4.03 (Synergy Software). The equation shown in Figure S1 was used to analyze the chymotryptic-like catalytic activity and catalytic activation of the 20S proteasome. For the determination of the first-order inactivation rate constants, equations were used that contained either two exponential terms in case of Z-LLY-Ketoaldehyde, or two exponential terms plus a linear term for epoxyketones (Oprozomib and Dihydroeponemycin). The first of the two exponential terms accounts for the catalytic activation, whereas the second exponential term signifies the catalytic inactivation by inhibitory action. The linear term in case of the epoxyketones was used to describe account for the residual activity of the proteasome after inactivation.

Supplementary Text (related to the electronic structure calculations)

Choice of system for simulation

The system of choice for our calculations was the Dihydroeponemycin inhibitor. The reason for this choice is twofold. On one hand, the chosen system allows us to compare 6-ring and 7-ring formation pathways on the same footing. Secondly, the spectating hydroxyl moiety of Dihydroeponemycin, according to crystal structure data, displaces the catalytic H2O-3, and should be able to perform a similar role. In our calculations, this comes as a benefit, since it is easier to model the hydroxyl group (it has inherently less degrees of freedom than a single water molecule) (Figure S8).

Formation of the tetrahedral intermediate

The first reaction step in the inhibition process should correspond to the formation of a tetrahedral intermediate, through the nucleophilic attack of the hydroxyl moiety of the threonine residue to the keto-carbon of the inhibitor. The model (cluster) system used is depicted in Figure S8a. The neighboring residues Lys33, Ser130 and Asp17 were included, as well as the NUK water and a further solvent molecule, which was added to complete the hydrogen bond network to the Ser130 residue. There is no conserved water in the crystal structures at this position, but there is enough space available to accommodate one. The side chains of included were truncated at the α carbons. During all optimizations, the position of the latter carbons was kept fixed in the crystallographic coordinates (taken from the crystal structure data of the $Mg(OAc)_2$ soaked crystals of the Dihydroeponemycin inhibition product). All remaining atoms were moved in stationary point searches and reaction path calculations.

Reaction paths were computed by performing constrained optimizations, keeping the distance between the nucleophilic oxygen and the keto carbon fixed, while optimizing all other degrees of freedom in the system (aside the constraint on the cartesian coordinates of the α carbons). A connected path was obtained, whereby the reaction proceeds by a proton transfer from the Thr1 γ-OH to the Lys33 ε-amine, followed by nucleophilic attack of the hydroxide. Two groups are particularly important for the energetics of this pathway. On the one side, Asp17 favors the formation of the ε-NH_3^+ group in the lysine. Test calculations carried out without the aspartate lead to either very high barriers or no connected paths overall. The other important element is the NUK water. Although in our optimized pathways we did not observe a proton transfer to the forming hydroxide, one

does observe the formation of a strong hydrogen bond. Our model would require, most likely, a larger active site in order to describe the final protonation step. A reaction profile is given in Figure S9.

6-ring and 7-ring pathways

In a further set of calculations, we compared the energetics for the pathway leading to 6- and 7-ring formation. We again take Dihydroeponemycin as inhibitor and the model for the active site is shown in Figure S8b. A smaller model system is used, focusing on the Thr1 amine and the 3-ring of the inhibitor. A water molecule was added, in order to complete the hydrogen bond network between the Dihydroeponemycin methanolic OH group and the Thr1 reactive NH_2 group. This role is most likely filled by Ser170. The Thr1 is truncated by a dimethylamine, thereby avoiding any acidic protons at this position. It is visible in the crystal structures that the NH in the backbone is involved in a hydrogen bond to a neighboring residue. However, in our limited model, since the latter residue is left out, the proton would be able to coordinate to the free water molecule. This was observed in multiple occasions during our studies. In order to avoid this, the H atom was replaced by a methyl, thereby turning the site inaccessible to further hydrogen bonds. The NUK water molecule was not included in this model since it is located on the opposite stereoface of the ring. Lys33, Asp17 and Ser130 had little impact in the barriers and were also neglected. In the case of cluster calculations, and in order to better compare two different pathways, it is often best to limit the size of the model to the direct participants in the reaction, in order to avoid a contamination of the results by fortuitous conformation changes of spectating atoms.

The reactive pathways were obtained by performing constrained optimizations, keeping the distance between the nitrogen and the target carbon in the inhibitor. The two reaction pathways (6- and 7-ring formation) are given in Figure S10 (B3LYP-D3/def2-SVP electronic energies). The highest points in energy along the path were then taken as first structure guesses for transition state optimization, following the closest mode to the N-C stretch. Both pathways stem from the same starting structure, the tetrahedral intermediate, with the amine group facing the epoxide.

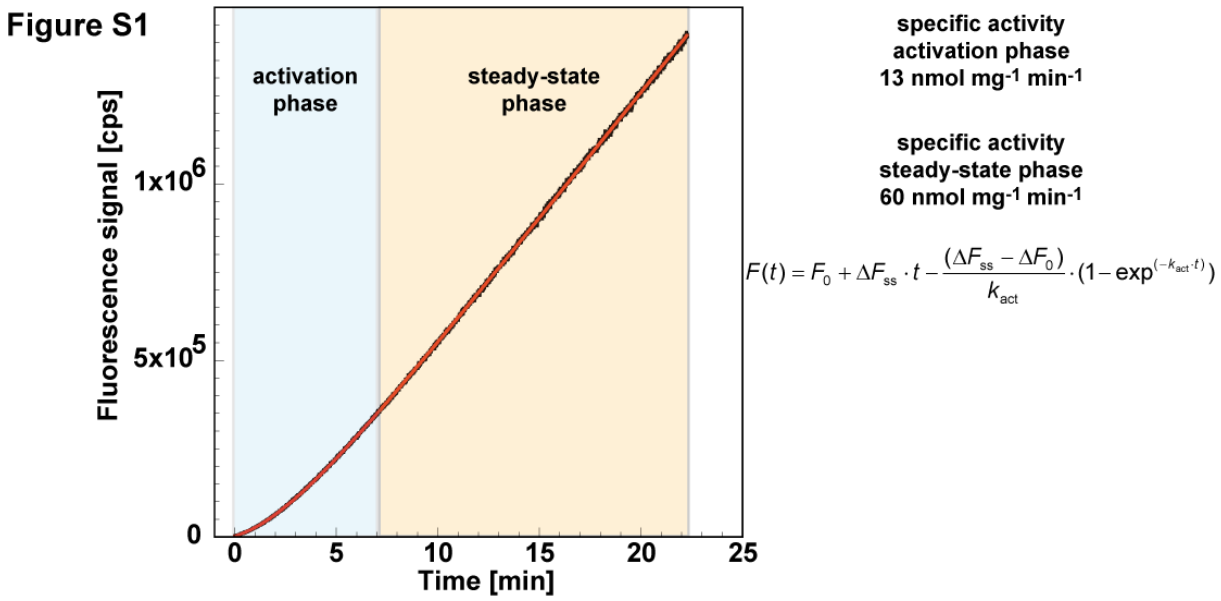

Fig. S1. Enzymatic characterization of proteasome catalytic activity

Measurements were performed as described in methods. The left panel depicts a typical kinetic experiment, where the increase in fluorescence signal of the AMC released by proteolytic cleavage is plotted against time. The blue window signifies an activation phase in enzymatic peptide cleavage, whereas the pink window represents the steady-state phase. In the right panel the specific activities for the human 20S proteasome purified by our method are indicated for the pre-steady-state (prior to activation) or and the steady-state phases, respectively. The equation shown in the right panel was used to perform fits (in red) against the experimental data (black). F_0 designates the initial fluorescence, ΔF_{ss}: fluorescence increase in the steady-state part of the measurement, k_{act}: the rate constant. The exponential term with the rate constant k_{act} is used to describe the activation phase of the reaction.

Figure S2

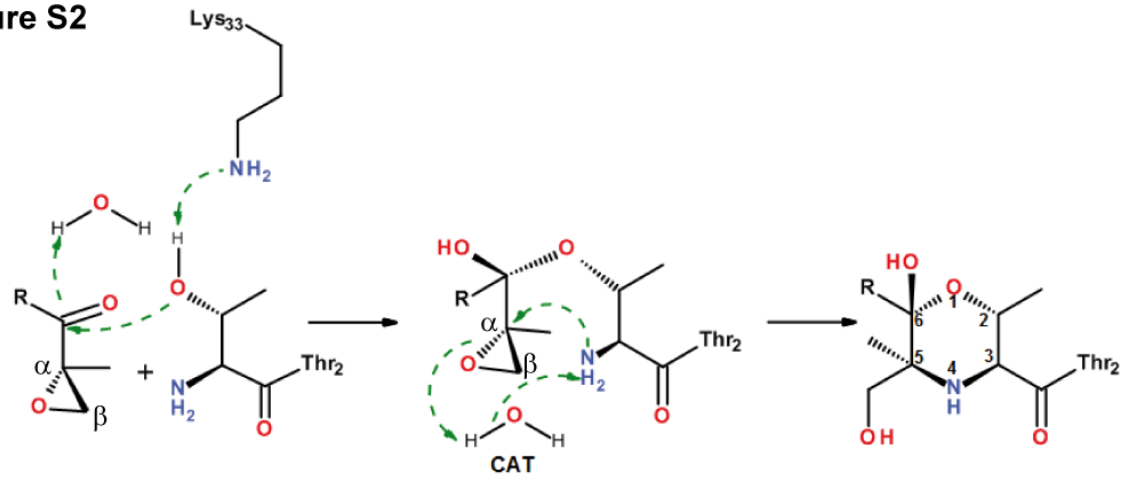

Fig. S2. Inhibition mechanism for epoxyketones as proposed thus far.

In the mechanism proposed by Groll et al. (14), the Thr1-Oγ initially reacts with the ketone (left) to form a hemiacetal (middle). The N-terminal amine of Thr1 then reacts with the epoxide α-carbon atom, giving rise to 1,4-morpholine (6-membered) linkage in the inhibited proteasome active site (right).

Figure S3

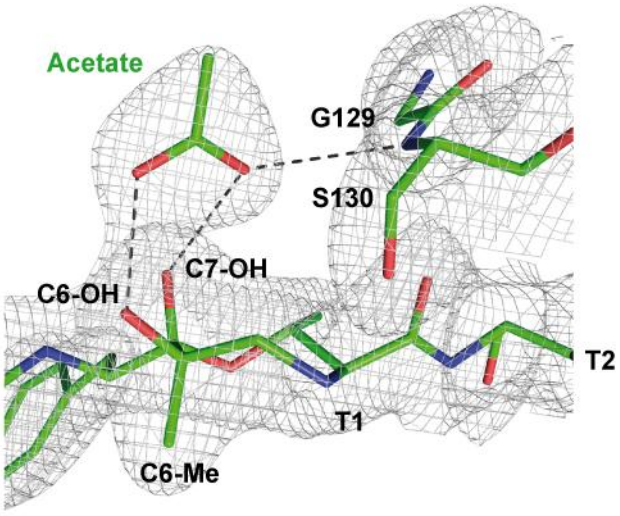

Fig. S3. Exchange of Chloride for Acetate does not affect formation of a 7-membered, 1,4-oxazepane linkage.

When 20S proteasome crystals were soaked with Mg(OAc)2 prior to Oprozomib, the linkage formed in the proteasome active site represents a 7-membered ring. In addition, an acetate molecule is visualized, which is hydrogen-bonded to the C6-OH and C7-OH of the 1,4-oxazepane ring. In addition, it also forms a hydrogen bond to the main chain amide of Ser130.

Figure S4

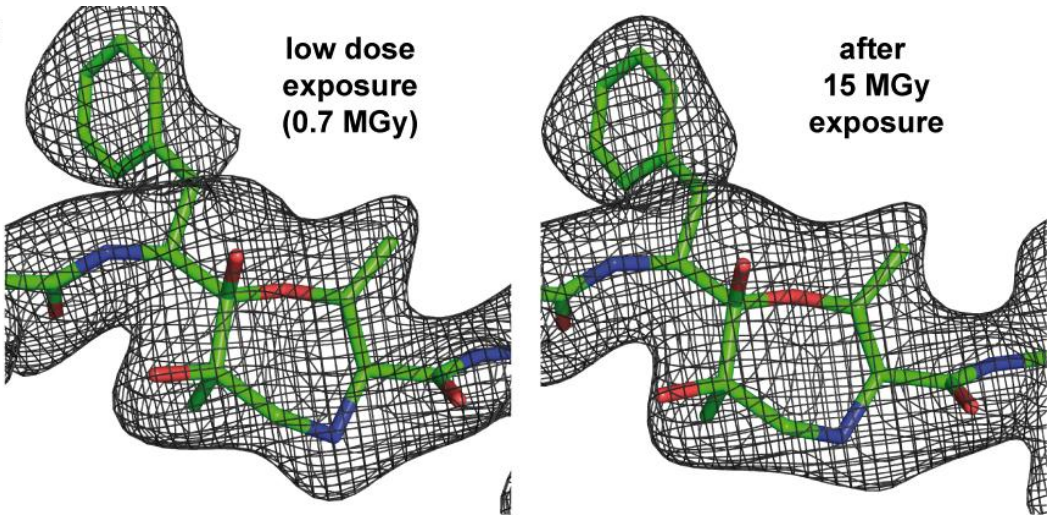

Fig. S4. Formation of the 1,4-oxazepane 7-membered ring linkage is not a consequence of radiochemistry during X-ray data collection.

Shown are electron density maps and the 7-membered ring linkage from a low-dose dataset (0.7 MGy, left panel) and after exposure to 15 MGy dose (right panel). No obvious differences are discernable, allowing the conclusion that radiochemistry is not the source for the 1,4-oxazepane ring.

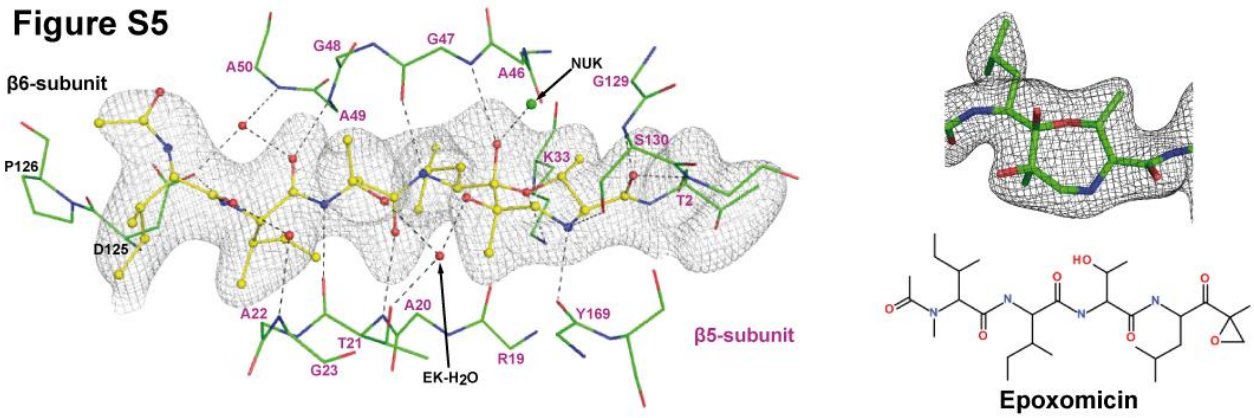

Fig. S5. Validation of 1,4-oxazepane linkage formation by the Epoxomicin-human 20S proteasome co-crystal structure.

The left panel illustrates the β5 active site inhibited by Epoxomicin, along with an omit map contoured at 4σ for the inhibitor, covalent linkage and β5Thr2. The main chain segments of β5 residues 2, 19-21, 33, 45-50, 129-131, 169,170 and β6 125,126 are indicated along with the β5 side chains of Thr2, Thr23, Lys33, Ser130 and the side chains of β6 Asp125, Pro126 as sticks (green carbon); Inhibitor, red oxygen and blue nitrogen; see picture for amino acid description). The NUK chloride is shown as a green dot. Dashed lines signify hydrogen bonds (≤3.2 Å distance). The top right panel a close-up view of the inhibitor-Thr1 linkage is shown, along with an omit map contoured at 6σ (green carbon, red oxygen and blue nitrogen). The right bottom panel the chemical structure of Epoxomicin is depicted.

Figure S6

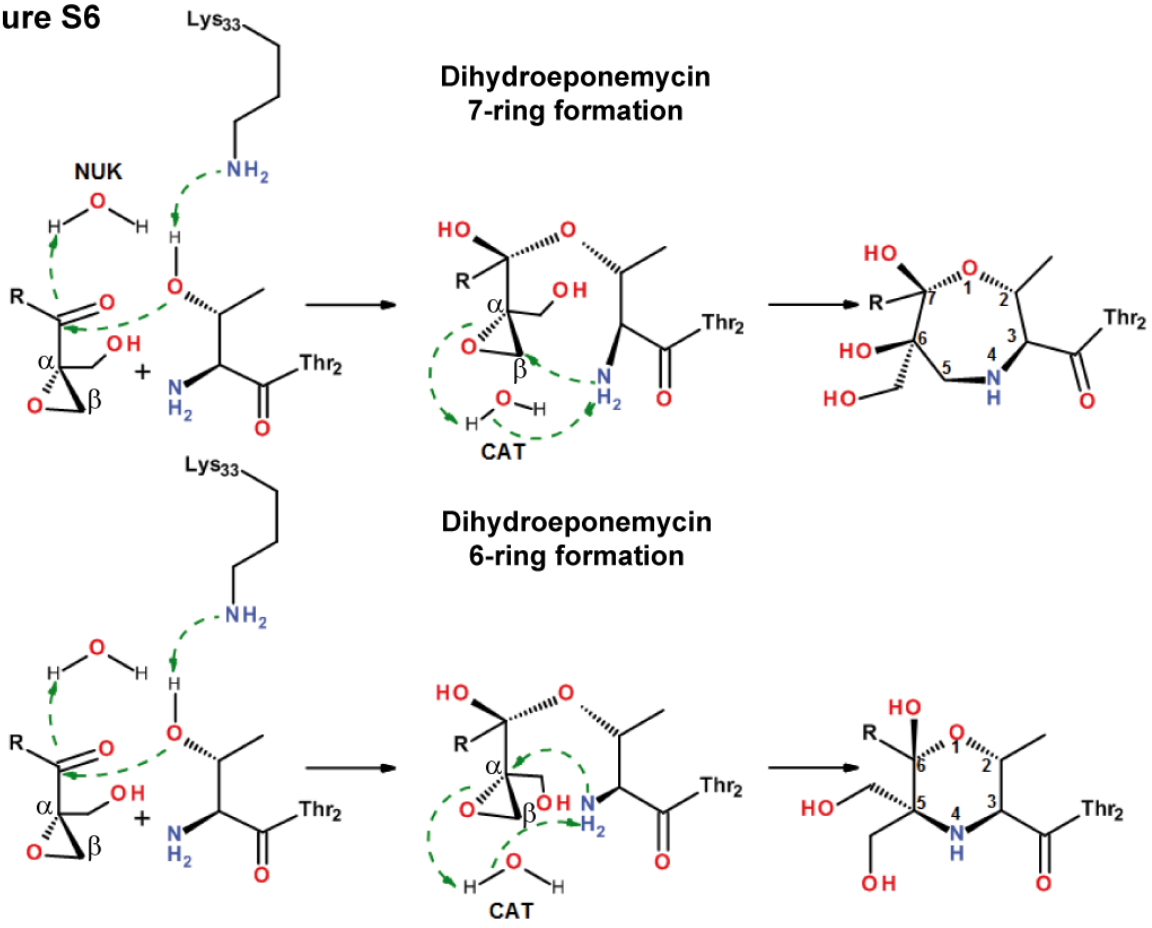

Fig. S6. Comparison of 6- and 7-ring forming reaction mechanisms for Dihydroeponemycin.

The top panel depicts a reaction mechanism, which leads to the formation of a 1,4-oxazepane 7-membered ring linkage in the inhibited proteasome active site. In the bottom panel a reaction mechanism is shown, which gives rise to a 1,4-morpholine 6-membered ring linkage. Note that in the upper case, the Thr1 N-terminal amine is involved in a nucleophilic reaction with the epoxide β-carbon atom, whereas in the bottom case it attacks the epoxide α-carbon atom. Note also that 1,4-morpholine linkage would give rise

to a non-chiral center at C5 position of the linkage, which would contain two methanolic groups.

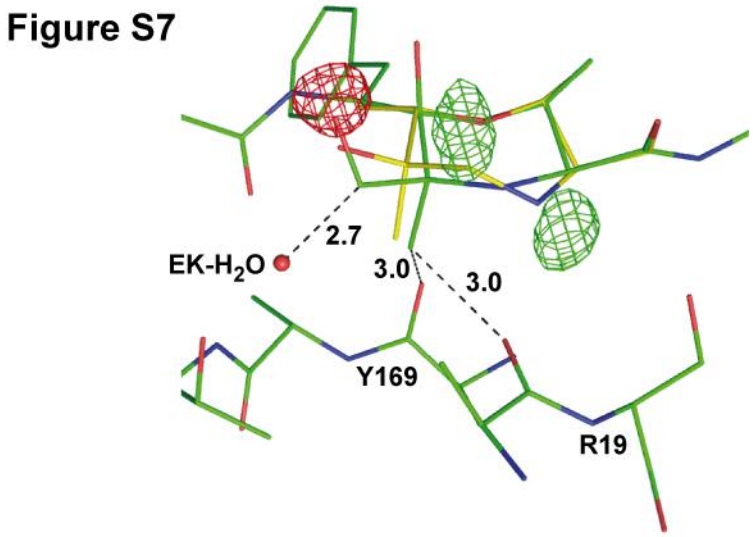

Fig. S7. Competitive refinement of 1,4-morpholine (6-ring) versus 1,4-oxazepane (7-ring) linkage.

Our attempts to model the electron density in the active site of β5 subunits in Oprozomib-soaked crystals by a 1,4-morpholine (6-) ring structure were unsuccessful. 1,4-morpholine linkage conjugates refinement resulted in a severely distorted molecular geometry (green carbon model) characterized by the elongation of the N4-carbon bonds by 0.1-0.2 Å, shortening of the C5-alcohol carbon bond by 0.1 Å and deviation of the C5-methylalcohol bond angle by -20 degrees from the expected value. Additionally, the C5-methyl carbon atom exhibited a van der Waals distance of 3.0 Å to R19 and Y169 main chain oxygen atoms, which is too close and would result in a repulsive interaction. Moreover, strong negative difference density peaks in difference maps contoured at 5σ levels at the C5 methanol oxygen of the 1,4-morpholine ring model, as well as positive density peaks contoured at 4.5 σ levels close to positions 4 and 5 of our 1,4-oxazepane

ring model remained after this 1,4-morpholine ring refinement. In contrast, no residual difference (neither negative nor positive) density was present in the refined 1,4-oxazepane linkage in density maps contoured above 2.3 σ. Depicted is a mFo-DFc map contoured at +4 σ (green) and -4 σ (red). For comparison, the model with the 1,4-oxazapane linkage as depicted in Figure 3A is shown with carbon colored in yellow.

Figure S8

A) **B)**

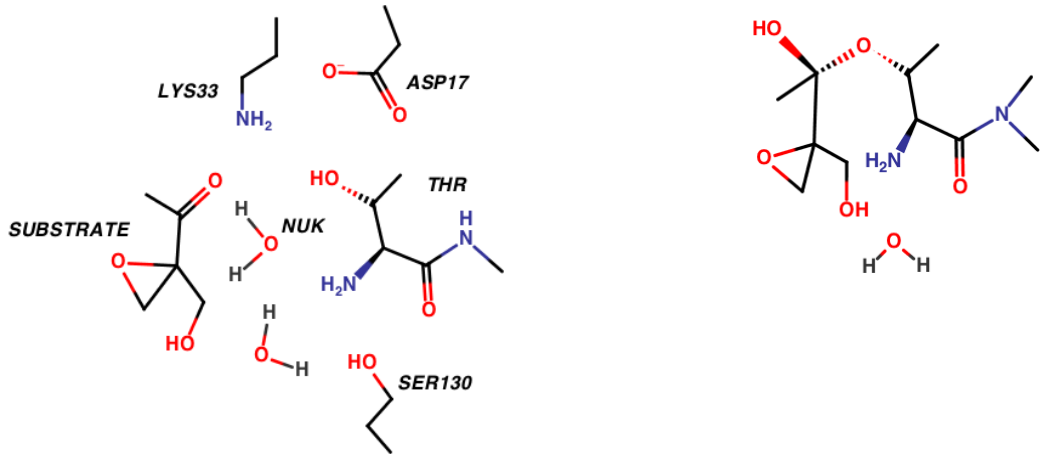

Fig. S8. Model systems used for the computation of (A) tetrahedral intermediate formation (B) ring formation.

Figure S9

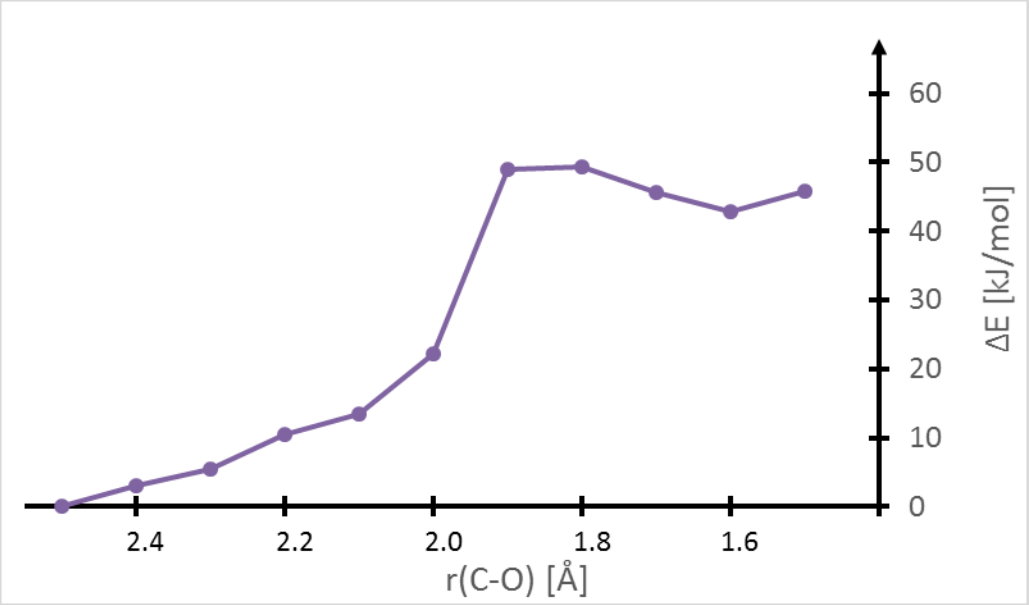

Fig. S9. Electronic energy differences in the computed pathway for the nucleophilic attack at the keto carbon.

The cluster model used is shown in Fig. S8 a). The α carbon atoms of the capped residues were kept fixed. The distance between the nucleophilic oxygen in Thr1 and the keto carbon in the inhibitor r(C-O) was varied optimizing all other coordinates. The model system chosen is not large enough to describe the final protonation of the forming hydroxyl group at the inhibitor molecule. This should lead to an overestimation of both the energy barrier and the final products energy.

Figure S10

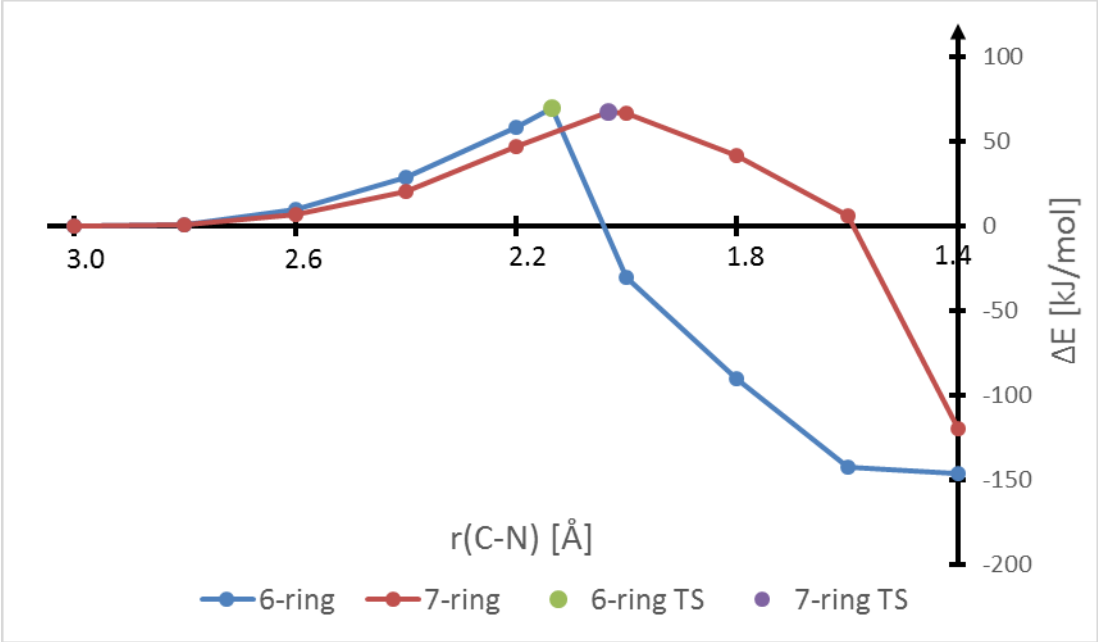

Fig. S10. Electronic energy differences comparing the 6- and 7-ring formation pathways in the dihydroeponemycin inhibitor case.

The r(C-N) distance corresponds to the distance in the forming bond, and therefore refers to two different carbons.

Table S1.

Buffers for protein purification, crystallization, crystal stabilization, crystal dehydration and enzymatic assays

Purification buffer:	0.05 M BisTris pH 6.5, 0.05 M KCl, 0.01 M $MgCl_2$, 0.01 M β-Glycerophosphate
Crystallization buffer:	0.1 M BisTris pH 6.5, 0.2 M $MgCl_2$, 10 % (w/v) PEG3350
Crystal stabilization buffer:	0.1 M BisTris pH 6.5, 0.2 M $MgCl_2$, 20 % (w/v) PEG 3350
Crystal dehydration buffer:	0.1 M BisTris pH 6.5, 0.2 M $MgCl_2$, 25 % (w/v) PEG 3350, 20% (v/v) MPD
Enzyme activity buffer:	0.05 M BisTris pH 6.75, 1 mM EDTA, 0.01% (w/v) SDS

Table S2. Crystallographic data collection and refinement statistics.

Tag	Native	Native	Oprozomib	Oprozomib	Epoxomycin	Dihydroeponemycin	Z-LLY-ketoaldehyde	Bortezomib	Ixazomib	Delanzomib
PDB ID	5LE5	5LEX	5LEY	5LEZ	5LF0	5LF1	5LF6	5LF3	5LF7	5LF4
Divalent salt	$MgCl_2$	$Mg(OAc)_2$	$MgCl_2$	$Mg(OAc)_2$	$MgCl_2$	$MgCl_2$	$MgCl_2$	$MgCl_2$	$MgCl_2$	$MgCl_2$
Space group	$P2_12_12_1$									
Unit cell										
a (Å)	113.4	113.9	113.4	113.9	113.1	113.9	113.9	113.4	113.4	114.4
b (Å)	202.8	203.1	202.7	203.2	202.4	203.5	203.5	202.7	202.6	202.8
c (Å)	316.0	316.0	315.1	315.2	314.8	316.0	315.6	314.9	314.5	314.3
Data collection										
Wavelength (Å)	0.976									
Resolution range (Å)	107-1.80 (1.90-1.80)	50-2.20 (2.28-2.20)	170-1.90 (2.00-1.90)	50-2.19 (2.27-2.19)	107-2.41 (2.50-2.41)	50-2.0 (2.07-2.00)	50-2.07 (2.15-2.07)	157-2.10 (2.20-2.10)	94-2.00 (2.10-2.00)	50-1.99 (2.06-1.99)
No. of reflections	8923661	2519654	2653718	2510786	2519995	4381423	2792074	2017022	3047303	4210019
No. of unique reflections	633728	366080	526170	351230	262073	464668	403247	393306	459417	462522
Completeness (%)	99.9 (99.7)	99.2 (98.1)	97.5 (99.4)	99.3 (94.3)	99.9 (99.6)	99.8 (98.3)	96.4 (72.3)	98.7 (89.1)	99.8 (99.6)	99.1 (90.0)
<I/SigI>	18.5(0.9)	13.0 (0.9)	15.3 (0.8)	15.2 (1.1)	13.1 (0.8)	12.2 (1.0)	12.9 (0.6)	12.4 (0.9)	14.6 (1.0)	11.3 (1.0)
$CC_{1/2}$	1.00 (0.32)	1.00 (0.36)	1.00 (0.24)	1.00 (0.40)	1.00 (0.28)	1.00 (0.39)	0.99 (0.22)	1.00 (0.26)	1.00 (0.29)	0.99 (0.31)
$R_{r.i.m.}$	0.026 (0.71)	0.039 (0.87)	0.041 (1.03)	0.036 (0.81)	0.060 (1.06)	0.038 (0.69)	0.043 (1.0)	0.052 (0.87)	0.041(1.1)	0.045 (0.8)
Refinement										
Rwork	0.184	0.176	0.189	0.181	0.168	0.175	0.185	0.183	0.182	0.184
Rfree	0.213	0.220	0.224	0.222	0.227	0.209	0.226	0.225	0.215	0.217
No. of atoms										
Protein	48205	48134	48208	48372	48372	48302	48219	48331	48272	48272
Ligand/solvent	3712	3493	3756	3882	3385	3839	3718	3888	3809	3794
Average B values ($Å^2$)										
Protein	46	67	49	65	67	51	55	52	53	52
Inhibitor	-	-	34	47	48	39	45	42	49	33
Metals	36	59	42	57	54	42	45	43	48	46
Cl ions	51	-	56	-	79	56	68	60	63	65
Water	48	64	51	64	62	54	59	55	58	60
Wilson	41	57	44	56	59	46	49	46	46	42
R.m.s.d. bond length (Å)	0.018	0.015	0.016	0.015	0.018	0.014	0.013	0.014	0.013	0.012
R.m.s.d. bond angles (Å)	1.92	1.72	1.80	1.75	1.89	1.71	1.65	1.72	1.68	1.642
Ramachandran % most favoured /favoured	95.88/3.06	95.60/3.29	95.58/3.30	95.24/3.45	95.91/2.88	95.68/3.16	95.49/3.35	95.67/3.12	95.62/3.24	95.88/2.99

Values in parenthesis denote values for the highest resolution shell.

Number of unique reflections used in refinement is shown. No rejections were applied.

Movie S1

This movie illustrates the entire calculated reaction pathway for the formation of the 1,4-oxazepane 7-membered ring linkage with Dihydroeponemycin.

Movie S2

This movie illustrates the entire calculated reaction pathway for the formation of the 1,4-morpholine 6-membered ring linkage with Dihydroeponemycin.

References

1. M. Bochtler, L. Ditzel, M. Groll, C. Hartmann, R. Huber, The proteasome. *Annu. Rev. Biophys. Biomol. Struct.* **28**, 295–317 (1999). Medline doi:10.1146/annurev.biophys.28.1.295

2. E. Kish-Trier, C. P. Hill, Structural biology of the proteasome. *Annu Rev Biophys* **42**, 29–49 (2013). Medline doi:10.1146/annurev-biophys-083012-130417

3. A. Ciechanover, The ubiquitin-proteasome proteolytic pathway. *Cell* **79**, 13–21 (1994). Medline doi:10.1016/0092-8674(94)90396-4

4. D. Finley, Recognition and processing of ubiquitin-protein conjugates by the proteasome. *Annu. Rev. Biochem.* **78**, 477–513 (2009). Medline doi:10.1146/annurev.biochem.78.081507.101607

5. M. Groll, L. Ditzel, J. Löwe, D. Stock, M. Bochtler, H. D. Bartunik, R. Huber, Structure of 20S proteasome from yeast at 2.4 A resolution. *Nature* **386**, 463–471 (1997). Medline doi:10.1038/386463a0

6. W. Harshbarger, C. Miller, C. Diedrich, J. Sacchettini, Crystal structure of the human 20S proteasome in complex with carfilzomib. *Structure* **23**, 418–424 (2015). Medline doi:10.1016/j.str.2014.11.017

7. P. C. da Fonseca, E. P. Morris, Cryo-EM reveals the conformation of a substrate analogue in the human 20S proteasome core. *Nat. Commun.* **6**, 7573 (2015). Medline doi:10.1038/ncomms8573

8. A. Chari, D. Haselbach, J. M. Kirves, J. Ohmer, E. Paknia, N. Fischer, O. Ganichkin, V. Möller, J. J. Frye, G. Petzold, M. Jarvis, M. Tietzel, C. Grimm, J. M. Peters, B. A. Schulman, K. Tittmann, J. Markl, U. Fischer, H. Stark, ProteoPlex: Stability optimization of macromolecular complexes by sparse-matrix screening of chemical space. *Nat. Methods* **12**, 859–865 (2015). Medline doi:10.1038/nmeth.3493

9. E. M. Huber, M. Basler, R. Schwab, W. Heinemeyer, C. J. Kirk, M. Groettrup, M. Groll, Immuno- and constitutive proteasome crystal structures reveal differences in substrate and inhibitor specificity. *Cell* **148**, 727–738 (2012). Medline doi:10.1016/j.cell.2011.12.030

10. E. M. Huber, W. Heinemeyer, X. Li, C. S. Arendt, M. Hochstrasser, M. Groll, A unified mechanism for proteolysis and autocatalytic activation in the 20S proteasome. *Nat. Commun.* **7**, 10900 (2016). Medline doi:10.1038/ncomms10900

11. E. M. Huber, W. Heinemeyer, M. Groll, Bortezomib-resistant mutant proteasomes: Structural and biochemical evaluation with carfilzomib and ONX 0914. *Structure* **23**, 407–417 (2015). Medline doi:10.1016/j.str.2014.11.019

12. S. D. Demo, C. J. Kirk, M. A. Aujay, T. J. Buchholz, M. Dajee, M. N. Ho, J. Jiang, G. J. Laidig, E. R. Lewis, F. Parlati, K. D. Shenk, M. S. Smyth, C. M. Sun, M. K. Vallone, T. M. Woo, C. J. Molineaux, M. K. Bennett, Antitumor activity of PR-171, a novel irreversible inhibitor of the proteasome. *Cancer Res.* **67**, 6383–6391 (2007). Medline doi:10.1158/0008-5472.CAN-06-4086

13. T. A. Grigoreva, V. G. Tribulovich, A. V. Garabadzhiu, G. Melino, N. A. Barlev, The 26S proteasome is a multifaceted target for anti-cancer therapies. *Oncotarget* **6**, 24733–24749 (2015). Medline doi:10.18632/oncotarget.4619

14. M. Groll, K. B. Kim, N. Kairies, R. Huber, C. M. Crews, Crystal structure of epoxomicin: 20S proteasome reveals a molecular basis for selectivity of α',β'-epoxyketone proteasome inhibitors. *J. Am. Chem. Soc.* **122**, 1237–1238 (2000). doi:10.1021/ja993588m

15. J. F. Lynas, P. Harriott, A. Healy, M. A. McKervey, B. Walker, Inhibitors of the chymotrypsin-like activity of proteasome based on di- and tri-peptidyl α-keto aldehydes (glyoxals). *Bioorg. Med. Chem. Lett.* **8**, 373–378 (1998). Medline doi:10.1016/S0960-894X(98)00030-4

16. M. A. Gräwert, N. Gallastegui, M. Stein, B. Schmidt, P. M. Kloetzel, R. Huber, M. Groll, Elucidation of the α-keto-aldehyde binding mechanism: A lead structure motif for proteasome inhibition. *Angew. Chem. Int. Ed. Engl.* **50**, 542–544 (2011). Medline doi:10.1002/anie.201005488

17. R. C. Kane, A. T. Farrell, R. Sridhara, R. Pazdur, United States Food and Drug Administration approval summary: Bortezomib for the treatment of progressive multiple myeloma after one prior therapy. *Clin. Cancer Res.* **12**, 2955–2960 (2006). Medline doi:10.1158/1078-0432.CCR-06-0170

18. M. Shirley, Ixazomib: First global approval. *Drugs* **76**, 405–411 (2016). Medline doi:10.1007/s40265-016-0548-5

19. M. K. Bennett, C. J. Kirk, Development of proteasome inhibitors in oncology and autoimmune diseases. *Curr. Opin. Drug Discov. Devel.* **11**, 616–625 (2008). Medline

20. J. D. Dignam, R. M. Lebovitz, R. G. Roeder, Accurate transcription initiation by RNA polymerase II in a soluble extract from isolated mammalian nuclei. *Nucleic Acids Res.* **11**, 1475–1489 (1983). Medline doi:10.1093/nar/11.5.1475

21. W. Kabsch, Xds. *Acta Crystallogr. D Biol. Crystallogr.* **66**, 125–132 (2010). Medline doi:10.1107/S0907444909047337

22. P. Emsley, B. Lohkamp, W. G. Scott, K. Cowtan, Features and development of Coot. *Acta Crystallogr. D Biol. Crystallogr.* **66**, 486–501 (2010). Medline doi:10.1107/S0907444910007493

23. A. A. Lebedev, P. Young, M. N. Isupov, O. V. Moroz, A. A. Vagin, G. N. Murshudov, JLigand: A graphical tool for the CCP4 template-restraint library. *Acta Crystallogr. D Biol. Crystallogr.* **68**, 431–440 (2012). Medline doi:10.1107/S090744491200251X

24. G. N. Murshudov, A. A. Vagin, E. J. Dodson, Refinement of macromolecular structures by the maximum-likelihood method. *Acta Crystallogr. D Biol. Crystallogr.* **53**, 240–255 (1997). Medline doi:10.1107/S0907444996012255

25. A. D. Becke, Density-functional thermochemistry. 3. The role of exact exchange. *J. Chem. Phys.* **98**, 5648–5652 (1993). doi:10.1063/1.464913

26. S. Grimme, S. Ehrlich, L. Goerigk, Effect of the damping function in dispersion corrected density functional theory. *J. Comput. Chem.* **32**, 1456–1465 (2011). Medline doi:10.1002/jcc.21759

27. C. Lee, W. Yang, R. G. Parr, Development of the Colle-Salvetti correlation-energy formula into a functional of the electron density. *Phys. Rev. B Condens. Matter* **37**, 785–789 (1988). Medline doi:10.1103/PhysRevB.37.785

28. F. Weigend, R. Ahlrichs, Balanced basis sets of split valence, triple zeta valence and quadruple zeta valence quality for H to Rn: Design and assessment of accuracy. *Phys. Chem. Chem. Phys.* **7**, 3297–3305 (2005). Medline doi:10.1039/b508541a

29. E. R. Johnson, A. D. Becke, A post-Hartree-Fock model of intermolecular interactions: Inclusion of higher-order corrections. *J. Chem. Phys.* **124**, 174104 (2006). Medline doi:10.1063/1.2190220

30. A. Klamt, G. Schuurmann, Cosmo: A new approach to dielectric screening in solvents with explicit expressions for the screening energy and its gradient. *Journal of the Chemical Society-Perkin Transactions* **2**, 799–805 (1993). doi:10.1039/P29930000799

31. M. R. A. Blomberg, T. Borowski, F. Himo, R. Z. Liao, P. E. M. Siegbahn, Quantum chemical studies of mechanisms for metalloenzymes. *Chem. Rev.* **114**, 3601–3658 (2014). Medline doi:10.1021/cr400388t

32. F. Neese, The ORCA program system. *Wiley Interdisciplinary Reviews-Computational Molecular Science* **2**, 73–78 (2012). doi:10.1002/wcms.81

33. R. L. Stein, F. Melandri, L. Dick, Kinetic characterization of the chymotryptic activity of the 20S proteasome. *Biochemistry* **35**, 3899–3908 (1996). Medline doi:10.1021/bi952262x